

Titles

Quasi-monoenergetic and tunable x-rays from a laser-driven Compton light source**

Authors

N. D. Powers, I. Ghebregziabher, G. Golovin, C. Liu, S. Chen, S. Banerjee, J. Zhang, and
D. P. Umstadter*

Affiliations

Department of Physics and Astronomy, University of Nebraska-Lincoln, Lincoln 68588
USA

****Note:** This manuscript is the pre-print version (9/14/13 submission) of an article published in *Nature Photonics* ([DOI 10.1038/nphoton.2013.314](https://doi.org/10.1038/nphoton.2013.314)).

Introductory Paragraph

The maximum achievable photon energy of compact conventional Compton scattering x-ray light sources is currently limited by the maximum permissible field gradient of conventional electron accelerators^{1,2}. An alternate compact Compton x-ray source architecture with no such limitation is based instead on a high-field-gradient laser-wakefield accelerator³⁻⁶. In this case, a single high power (100-TW) laser system generates intense laser pulses used for both electron acceleration and scattering. While such all-laser-based sources have been demonstrated in proof-of-principle experiments to be bright and energetic⁷⁻¹⁰, they have lacked until now several important distinguishing characteristics of conventional Compton sources. We now report the experimental demonstration of all-laser-driven Compton x-rays that are both quasi-monoenergetic (~50% FWHM) and tunable (~70 keV to >1 MeV). These performance improvements are highly beneficial for several important x-ray radiological applications^{2, 11-15}.

Main Text

Synchrotron x-ray light sources are in use for scientific research worldwide, because of their high brightness, tunability, and narrow photon-energy bandwidth. However, synchrotrons are typically large devices (stadium-sized), due to the size of their component electron accelerator and undulator. More compact (room-sized) synchrotron x-ray sources were recently reported^{1, 2}, which use an electromagnetic undulator, operating on the principle of inverse-Compton scattering, instead of a fixed-magnet undulator. The much higher frequency of optical laser light used in Compton scattering, relative to fixed magnet arrays, reduces the electron energy required to produce x-rays, which in turn reduces the required size of the electron accelerator. Even greater size reduction can be achieved when laser light is used to drive both the undulator and the electron accelerator^{7-10, 16}.

The RF-cavity-driven accelerator at Lawrence Livermore National Laboratory (LLNL), produces 478-keV x-ray beams with 12% spectral bandwidth, 16-ps inferred temporal duration, and a flux of 10^5 photons/shot, corresponding to 1.5×10^{15} photons $\text{s}^{-1} \text{mm}^{-2} \text{mrad}^{-2}$ (per 0.1% bandwidth) peak brilliance. Utilizing an laser-wakefield accelerator (LWFA)^{17, 18} with an accelerating field gradient $>1,000\times$ higher than conventional RF-cavity-driven accelerators, and thus is much more compact, we now demonstrate the production of quasi-monoenergetic x-rays that are 1,000x brighter with 10x more photons/shot. The increased brightness is due to the femtosecond pulse duration and micron-scale transverse size of LWFA electron beams and the x-rays they produce. This all-optical concept has been discussed theoretically^{3-6, 19}, and demonstrated in proof-of-

principle experiments⁷⁻¹⁰. However, the x-rays produced thus far have had large bandwidth and fixed energy, even though narrow-bandwidth and tunable LWFA-generated electron beams have already been demonstrated²⁰⁻²⁵. We now report x-rays from an LWFA-Compton light source that are not only bright and energetic but also possess several other distinguishing characteristics of synchrotron light: narrow-bandwidth (~50% FWHM) and central energy tunability over a wide range (~70 keV to >1 MeV).

The experiment was performed with the 100-TW, 800-nm *Diocles* laser at the University of Nebraska, Lincoln²⁶. The laser beam is divided into two synchronized light pulses by an optical beam splitter. As shown schematically in Fig. 1a, one pulse drives the LWFA, and the other acts as an undulator, by scattering from the electrons (see Methods). After interacting with the laser pulse, the electron beam is swept out of the x-ray path by a dipole magnet, and onto a charge-calibrated detector, which records the *e*-beam energy spectrum and angular divergence for each shot (Fig. 1b). The transverse spatial profile of the forward-directed x-ray beam is recorded by a calibrated detector array, Fig. 1c, placed outside of the vacuum system (see Methods).

The x-ray spectral bandwidth was directly measured by comparing the x-ray transmittances through a set of four Ross-filter²⁷ pairs, each pair being comprised of two elements of similar atomic number. The thickness of each pair (see Table 1) was designed such that the transmission curves closely match for all photon energies outside of the two *K* edges. The difference in transmitted signal through each pair (see Supplementary Fig. S1) was used to determine the number of photons with energies between the *K* edges. In order to accurately reconstruct the unfiltered x-ray spatial profile

(see Methods), the filters were arranged in a checkerboard pattern; allowing for multiple measurements across the cross-section of the beam. Fig. 2 shows the measured x-ray energy distribution, obtained using filters contained within 4.5 mrad of the beam center [slightly smaller than the 10-mrad full width at half maximum (FWHM) beam divergence]. The spectral distribution of the beam is centered at 66 ± 7 keV, with an energy spread of $\sim 50\%$ FWHM (fit by a Gaussian profile). By virtue of being peaked, rather than exponentially decaying with increasing energy (as in previous all-laser-driven Compton experiments⁷⁻¹⁰), this spectrum has the advantage of far fewer low-energy photons.

Assuming a collimated e -beam and narrow-bandwidth counter-propagating laser, the fractional bandwidth of the on-axis Compton-scattered spectrum is $\Delta E_\gamma / E_\gamma \approx 2 \Delta E_e / E_e$, where E_e and ΔE_e are the e -beam average energy and energy spread, and E_γ and ΔE_γ are the x-ray beam average energy and energy spread, respectively. The measured e -beam spectrum is peaked at 55 ± 3 MeV, see Fig. 2 (inset), with an energy spread of 22% (FWHM) (the spectral shape is well represented by a Gaussian fitting) and a 23-pC beam charge. The $\sim 6\%$ increase in the measured x-ray energy spread ($\sim 50\%$), as compared with the analytical prediction ($\sim 44\%$), is attributable to contributions from laser spectral bandwidth, scattering angle, divergence, and laser ponderomotive force, all of which in our case were small in comparison to the energy width contributed by the e -beam.

The experimental measurement of the x-ray bandwidth was compared with the predictions of a previously benchmarked numerical model⁶. The model simulates the

scattered x-ray spectrum, using as input parameters the measured *e*-beam characteristics, *i.e.*, energy spectrum and energy dependent divergence, represented by a six-dimensional phase space distribution. The model predicts an on-axis x-ray spectrum peaked at 71 keV, using as inputs our measured *e*-beam (Fig. 1b) and laser parameters (150-fs laser scattering pulse duration, focused intensity of 2×10^{17} W/cm²). Off-axis, the x-ray central energy decreases smoothly with increasing polar angle. Averaging the spectrum over the polar angles measured in the experiment results in an additional red-shift, with no significant change in the spectral width. The simulated spectrum, including contributions from all photons within the area used for Ross-filter analysis, predicts an averaged spectrum (see Fig. 2) that peaks at 64 keV, with 50% fractional bandwidth. Thus, the energy, the bandwidth, and the number of photons within the measured region (3×10^5 measured compared to 4.6×10^5 simulated), are all well within the uncertainty of the measurement.

The central x-ray energy can be tuned (Fig. 3) over one order-of-magnitude, by tuning the electron energy of the LWFA (see Supplementary Fig. S2), from ~50-300 MeV (see Methods). A different filter set and analysis method (see Methods) were required to measure the x-ray photon energy over this much larger range, due to limited working-range of the Ross-filter technique (see Supplementary Fig. S3). While the central energy could be measured by this method, the energy spread could not. For the ~70 shots in which the x-ray energy could be analyzed (see Fig. 3), the average central energy of the x-ray beam is observed to follow a quadratic scaling with the average *e*-beam central energy, as the latter was tuned. This agrees with the theoretically predicted $E_\gamma = 4\gamma^2 E_L$

scaling for photons backscattered on-axis by a single electron, where E_L and E_γ are the scattering and scattered photon energies, respectively, and γ is the relativistic Lorentz factor of the electron.

The reproducibility and stability of the x-rays were also computed, using a larger data set. X-ray beams were observed on >93% of shots (664 in total) when the scattering beam was present, illustrating the reproducibility of x-ray generation. For 56% of these shots, quasi-monoenergetic e -beams (energy spread $\lesssim 25\%$) were measured. From the above experimental results and theoretical analysis, we can infer that the x-rays on these shots were also quasi-monoenergetic (energy spread $\lesssim 50\%$). The measured electron energy spread, and thus inferred x-ray energy spread, was found to be the most stable for the lowest and highest electron energy settings, where >74% of the beams were quasi-monoenergetic (see Supplementary Fig. S2).

The x-ray photon number per shot was stable to within 60% of its average value, 1.7×10^6 (see Supplementary Fig. S4). The photon number, and thus photon flux, depends on three factors: scattering-laser beam intensity, degree of beam overlap, and e -beam charge. The stability was dominated by the stability of the e -beam charge which for this data set was stable to within 45% of its average value, 29 pC. Greater control of the flux can be expected by stabilizing the e -beam charge and adjusting the scattering-beam intensity.

The all-laser-driven architecture has several advantages. Besides smaller overall device size, the electron and scattering beam parameters are also better matched in size, and the pulses are better synchronized. These latter advantages have been shown to lead to high

peak x-ray brightness¹⁰, $\sim 3 \times 10^{18}$ photons $\text{s}^{-1} \text{mm}^{-2} \text{mrad}^{-2}$ (per 0.1% bandwidth) for Fig.

2. This is calculated using the measured beam divergence and photon number, and assuming a 30-fs x-ray pulse duration and 6- μm (rms) x-ray source size¹⁰. The 1-MeV photons in Fig. 3 have a peak brightness, $\sim 10^{19}$ photons $\text{s}^{-1} \text{mm}^{-2} \text{mrad}^{-2}$ (per 0.1% bandwidth), which is comparable to that found previously for a polychromatic x-ray beam of similar energy¹⁰.

The improved x-ray characteristics reported here should expand the reach of compact all-laser-driven Compton x-ray sources. For instance, narrow x-ray bandwidth, relative to bremsstrahlung, significantly reduces the amount of unwanted radiation in medical imaging. Consequently, radiographic image quality is improved¹², patient risk is decreased^{11, 13}, and beam-hardening effects are reduced². Additionally, photon energy-tunability can enhance radiographic imaging¹².

Further improvements in x-ray performance can be expected, by incorporating techniques used in conventional Compton sources and/or advances in LWFA technology. For instance, by using either higher scattering photon energy (achieved by harmonic conversion) or higher LWFA electron energy^{25, 28}, the x-ray energy should soon exceed the threshold for photo-nuclear disintegration (~ 10 MeV)^{14, 15}. Similarly, lower-bandwidth x-rays will result from using lower-bandwidth *e*-beams²⁰⁻²³. Finally, the control and stability of the x-ray energy will be substantially improved by recent advances in the degree of control and stability achieved for LWFA electron energy²⁴.

Methods Summary

Laser. The drive beam operated in the range of 1.3-1.7 J. The 33-fs drive pulse was focused with an f/14 parabolic mirror to a Gaussian spot size of 21 μm (FWHM). A spectral-phase closed loop and spatial-phase correction were used to optimize the drive beam focusability²⁶. The 150-fs, 130-170-mJ scattering beam was split from the drive beam, and then focused by a thin positive lens (f=1000 mm) to a Gaussian spot size of 17 μm (FWHM).

Undulator parameters. The scattering laser pulse was spatio-temporally overlapped with the *e*-beam at a position located 1.5 mm downstream of the accelerator exit, at an angle that was nearly backscattering (170 degrees). The laser had $N = 56$ cycles, and strength parameter of $a_0 = 0.3$.

Accelerator parameters. The accelerator consists of a drive laser beam, described above, and a gas nozzle. A dual-stage gas jet was employed, comprising an injector stage composed of 99:1 He:N₂ mixed gas ratio^{29,30}, and an accelerator stage, of pure He. The central energy is increased, within a given range, by increasing the plasma density of the accelerator stage while maintaining the gas jet length. Using a longer accelerator stage, results in an upshift in the tunable range. In these experiments, the plasma density of the 0.5-mm acceleration stage was scanned from 2×10^{17} - $2 \times 10^{18} \text{ cm}^{-3}$. For the two highest energy data points, shown in Fig. 3, the plasma density of a 2-mm nozzle was scanned from 1.2×10^{18} - $1.7 \times 10^{18} \text{ cm}^{-3}$ (see Supplementary Fig. S2). The accelerator design will be discussed in greater detail in a future publication.

Detection. Electron spectra were recorded by a 19-cm magnetic spectrometer, having a 0.8-T peak magnetic field. A map of the magnetic field, including fringe fields, was used to calculate the electron deflection as a function of energy. Electrons were detected by a $\text{Gd}_2\text{O}_2\text{S:Tb}$ phosphor screen (LANEX) imaged by a 12-bit CCD camera.

The x-rays were detected by cesium iodide (CsI) crystal array, composed of 40x40 1-mm square voxels, 1-cm deep, imaged by a 14-bit EMCCD camera. The voxels were separated by a 0.2-mm wide layer of epoxy. Cross-talk between voxels was measured using an x-ray tube source, and included in the analysis. The LANEX screen was placed outside of the x-ray beam path to allow simultaneous x-ray and e -beam measurements.

X-ray spectral measurement (Ross filters). A set of Ross filters was used to measure the x-ray spectral distribution, shown in Fig. 2. The filters were cut into 1.2-mm squares, and each aligned to cover a single detector voxel. Table 1 shows the filter pairs used, while Supplementary Fig. S1 shows the difference in transmission of each of the filter pairs. The width of each curve represents the bandwidth measured by each filter pair. Filter thicknesses were optimized to minimize the difference in transmitted signal outside the bandwidth.

The difference in signal level between two filters of a single Ross pair can be written explicitly as $\Delta S = \int_0^\infty X(E)\Omega(E)\Delta T(E)dE$, where E is the photon energy, S and T are the individual filter signal level and transmittance, respectively; $X(E)$ is the x-ray photon density, and $\Omega(E)$ is the detector response. Assuming the x-ray photon density has nearly linear slope within each Ross-pair bandwidth, the photon density can be written as

$X(E) = X^{\text{avg}}[1 + \beta (E - E^{\text{avg}})/\Delta E]$, where X^{avg} and E^{avg} are averaged photon density and energy within the Ross-pair bandwidth, ΔE is the Ross-pair bandwidth, and β is the spectrum steepness (ratio of the difference of photon density within the band to the averaged photon density). Finally, the averaged photon density can be found as $X^{\text{avg}} = \Delta S / \int_{E_1}^{E_2} \left[1 + \beta \frac{E - E^{\text{avg}}}{\Delta E}\right] \Omega(E) \Delta T(E) dE$. We used $\beta = 0$ to calculate the x-ray photon density, but included uncertainty in the slope in the error analysis as

$\sigma_\beta = \left| X_{\beta=\beta_{\text{max}}}^{\text{avg}} - X_{\beta=-\beta_{\text{max}}}^{\text{avg}} \right| / X_{\beta=0}^{\text{avg}}$. The upper limit on the photon density steepness ($\beta_{\text{max}} = 4$) was estimated from simulations. Other factors contributing to the error bars include: uncertainty in filter thickness, cross-talk between voxels, and filter bandgap leakage. Measurements of a polychromatic and a higher energy beam are shown in Supplementary Fig. S3, demonstrating the response of this technique to differing spectral distributions.

Unfiltered portions of the x-ray beam were used to reconstruct the x-ray beam profile by a 2D bi-harmonic spline interpolation. A map of the transmittance at each voxel was produced by dividing the measured signal by the reconstructed one.

Energy scaling analysis (continuum-attenuation filters). Tunability of the x-ray energy was measured over a wide range by using filters, chosen for their x-ray absorption properties in the continuum region (as opposed to near the *K*-edge, as with the Ross technique), including: aluminum (1.6 mm, 3mm, and 12 mm), copper (0.5 mm, 1 mm, 1.5 mm, 2 mm, 3 mm, 4.5 mm, and 6 mm), lead (1.6 mm), and uranium (0.175 mm). Filters were either cut into strips and overlaid in a loosely woven pattern, or separated in

a quad-filter or step-filter arrangement. The filter edges were aligned across a row or column of voxels, with at least two voxels between neighboring filters. For the two highest energy data points, 6.25-mm aluminium, 1.52-mm copper, and 6.24-mm lead filters were used.

Each point plotted in Fig. 3 is the average of several shots taken with the same accelerator parameters. The number of shots that could be analyzed was limited by the shot-to-shot fluctuation of the beam centering on the filters. The energy of quasi-monoenergetic x-ray beams ($<25\%$ energy spread for the corresponding e -beam) was analyzed only if the beam was centered on the appropriate filter set, thus providing adequate signal-to-noise ratio for accurate profile reconstruction. Since the beam energy is not correlated to the pointing of the beam, no bias was introduced in analyzing this subset of shots. The experimentally measured transmissions of each analyzed shot were compared to the simulated transmissions of all possible combinations of x-ray central energy and energy spread. Each combination represented a single test spectrum. The test spectrum with transmission values closest to the measured values, and with an energy spread $<150\%$ of the analytically predicted one, represented the central x-ray energy for that shot. Since the x-ray central energy could not be independently measured without some knowledge of the spectral shape, the measured e -beam energy distribution was used to determine the spectral shape of the x-ray distribution. The uncertainty in the central x-ray energy of a given shot was defined by the central energy of all test spectra with transmission values within the error of the measurement, and a bandwidth within 150%

of that determined from the e -beam energy distribution. Consistency in this method for all data points ensured accurate representation of the energy scaling.

Unfiltered portions of the beam were used to reconstruct the profile of the beam, by means of a 2-D Gaussian fitting in the filtered regions. Transmission values for the two highest energy sets could only be used to determine a lower limit for the x-ray central energy.

Simulation code. The scattered radiation from a single electron was obtained by solving the relativistic equations of motion⁶ for an electron in the intense laser field. The total scattered radiation was then obtained by integrating over the e -beam phase space distribution and focal volume of the laser field.

References

1. Albert, F. *et al.* Characterization and applications of a tunable, laser-based, MeV-class Compton-scattering gamma-ray source. *Phys. Rev. ST Accel. Beams* **13**, 070704 (2010).
2. Achterhold, K. *et al.* Monochromatic computed tomography with a compact laser-driven X-ray source. *Scientific Reports* **3**, 1313 (2013).
3. Catravas, P., Esarey, E. & Leemans, W. P. Femtosecond x-rays from Thomson scattering using laser wakefield accelerators. *Meas. Sci. Technol.* **12**, 1828-1834 (2001).
4. Umstadter D., He F., and Lau Y. U.S. Patent No. 7,321,604. (2008).
5. Esarey, E., Schroeder, C. B. & Leemans, W. P. Physics of laser-driven plasma-based electron accelerators. *Rev. Mod. Phys.* **81**, 1229-1285 (2009).
6. Ghebregziabher, I., Shadwick, B. A. & Umstadter, D. Spectral bandwidth reduction of Thomson scattered light by pulse chirping. *Phys. Rev. ST Accel. Beams* **16**, 030705 (2013).

7. Schwoerer, H., Liesfeld, B., Schlenvoigt, H. P., Amthor, K. U. & Sauerbrey, R. Thomson-Backscattered X Rays From Laser-Accelerated Electrons. *Phys. Rev. Lett.* **96**, 014802 (2006).
8. Ta Phuoc, K. *et al.* All-optical Compton gamma-ray source *Nat. Photonics* **6**, 308-311 (2012).
9. Mori, Y. *et al.* Head-On Inverse Compton Scattering X-rays with Energy beyond 10 keV from Laser-Accelerated Quasi-Monoenergetic Electron Bunches. *Appl. Phys. Expr.* **5**, 056401 (2012).
10. Chen, S. *et al.* MeV-Energy X Rays from Inverse Compton Scattering with Laser-Wakefield Accelerated Electrons. *Phys. Rev. Lett.* **110**, 155003 (2013).
11. Boone, J. M. & Seibert, J. A. A figure of merit comparison between bremsstrahlung and monoenergetic x-ray sources for angiography. *J. X-Ray Sci. Technol.* **4**, 334-345 (1994).
12. Carroll, F. E. Tunable Monochromatic X Rays: A New Paradigm in Medicine. *Am. J. Roentgenol.* **179**, 583-590 (2002).
13. Brenner, D. J. *et al.* Cancer risks attributable to low doses of ionizing radiation: Assessing what we really know. *Proc. Natl. Acad. Sci. U S A* **100**, 13761-13766 (2003).
14. Giulietti, A. *et al.* Intense γ -Ray Source in the Giant-Dipole-Resonance Range Driven by 10-TW Laser Pulses. *Phys. Rev. Lett.* **101**, 105002 (2008).
15. Habs, D. *et al.* Vision of nuclear physics with photo-nuclear reactions by laser-driven gamma beams. *Eur. Phys. J. D* **55**, 279-285 (2009).
16. Corde, S. *et al.* Femtosecond x rays from laser-plasma accelerators. *Rev. Mod. Phys.* **85**, 1-48 (2013).
17. Tajima, T. & Dawson, J. M. Laser Electron Accelerator. *Phys. Rev. Lett.* **43**, 267-270 (1979).
18. Esarey, E., Ride, S. K. & Sprangle, P. Nonlinear Thomson scattering of intense laser pulses from beams and plasmas. *Phys Rev E*. **48**, 3003-3021 (1993).
19. Hartemann, F. V. *et al.* Compton scattering X-ray sources driven by laser wakefield acceleration. *Phys. Rev. ST Accel. Beams* **10**, 011301 (2007).
20. Geddes, C. G. R. *et al.* High-quality electron beams from a laser wakefield accelerator using plasma-channel guiding. *Nature* **431**, 538-541 (2004).

21. Mangles, S. P. D. *et al.* Monoenergetic beams of relativistic electrons from intense laser-plasma interactions. *Nature* **431**, 535-538 (2004).
22. Faure, J. *et al.* A laser-plasma accelerator producing monoenergetic electron beams. *Nature* **431**, 541-544 (2004).
23. Brunetti, E. *et al.* Low Emittance, High Brilliance Relativistic Electron Beams from a Laser-Plasma Accelerator. *Phys. Rev. Lett.* **105**, 215007 (2010).
24. Gonsalves, A. J. *et al.* Tunable laser plasma accelerator based on longitudinal density tailoring. *Nat Phys* **7**, 862-866 (2011).
25. Banerjee, S. *et al.* Generation of tunable, 100-800 MeV quasi-monoenergetic electron beams from a laser-wakefield accelerator in the blowout regime. *Phys. Plasmas* **19**, 056703 (2012).
26. Liu, C. *et al.* Repetitive petawatt-class laser with near-diffraction-limited focal spot and transform-limited pulse duration. *Proc. SPIE 8599, Solid State Lasers XXII: Technology and Devices*, 859919 (2013).
27. Ross, P. A. A NEW METHOD OF SPECTROSCOPY FOR FAINT X-RADIATIONS. *J. Opt. Soc. Am.* **16**, 433-436 (1928).
28. Leemans, W. P. GeV electron beams from a centimetre-scale accelerator. *Nat. Phys.* **2**, 696-699 (2006).
29. Liu, J. S. *et al.* All-Optical Cascaded Laser Wakefield Accelerator Using Ionization-Induced Injection. *Phys. Rev. Lett.* **107**, 035001 (2011).
30. Pollock, B. B. *et al.* Demonstration of a Narrow Energy Spread, similar to 0.5 GeV Electron Beam from a Two-Stage Laser Wakefield Accelerator. *Phys. Rev. Lett.* **107**, 045001 (2011).

Acknowledgments We thank K. Brown, J. Mills, and C. Petersen for their contributions to the laser facility. We thank D. Haden and N. Cunningham from Nebraska Wesleyan University for their contributions with x-ray detector analysis. We thank C. Wilson, T. Anderson and D. Alexander from the University of Nebraska-Lincoln Electrical

Engineering department for precision cutting of Ross filters. This material is based upon work supported by U.S. Department of Energy: DE-FG02-05ER15663, Defense Threat Reduction Agency: HDTRA1-11-C-0001, Air Force Office for Scientific Research: FA9550-08-1-0232, and FA9550-11-1-0157, Department of Homeland Security: 2007-DN-077-ER0007-02, Defense Advanced Research Projects Agency: FA9550-09-1-0009 and USSTRATCOM: FA4600-12-D-9000. The views expressed here do not represent those of the sponsors.

Author Contributions Conception and design: DP, NP, SB, SC, IG, CL, GG;

Experiments: GG, NP, SB, SC, IG, CL, JZ; Data analysis: GG, IG, NP; Materials /

analysis tools: GG, IG, SB, NP; Writing: DP, NP.

Competing financial interests The authors declare no competing financial interests.

Author Information Reprints and permissions information is available at

www.nature.com/reprints. Correspondence and requests for materials should be

addressed to donald.umstadter@unl.edu.

Figure Legends

Figure 1: X-ray generation and detection. (a) Experimental setup (not to scale).

Electrons (green) are accelerated by the interaction of a drive laser beam (red, from left to right) with a plasma created within the plume of a dual-stage gas jet, and then deflected to a LANEX screen. A second laser pulse (red, from right to left) scatters from the e^- beam after the accelerator. The x-ray beam (purple) is recorded by a CsI detector after

passing through Ross filters arranged in a checkerboard pattern. **(b)** Raw LANEX image of electron beam spectrum. **(c)** Processed x-ray profile imaged through Ross filters.

Figure 2: X-ray bandwidth measurement. X-ray spectral distribution (■) measured, for a single shot, by the Ross-filter pairs. Horizontal error bars represent the spectral width of the filter pair, and vertical error bars represent the measurement error, including: uncertainty in filter thickness, cross-talk between voxels, and filter bandgap leakage. The simulated x-ray spectrum (—), obtained from experimentally measured *e*-beam spectrum (inset), is normalized by dividing by a factor of 1.4.

Figure 3: X-ray energy tuning. The measured x-ray central energy is plotted versus the measured *e*-beam central energy (■). Each point is an average of, from left to right, 25, 8, 8, 3, 5, 7, 8, and 5 selected shots (see Methods) taken with the same accelerator parameters. The error bars represent 80% confidence intervals, calculated using *t*-distribution of measurements in the set. The data is consistent with a $4\gamma^2$ scaling (---).

Supplementary Figure Legends

Figure S1: Ross-filter and CsI response curves. The transmission difference of filter pairs plotted (left axis) as a function of photon energy. Pair labeling matches that from Table 1. The CsI detector response curve (—) is also plotted (right axis) as a function of photon energy.

Figure S2: Control and stability of tunable quasi-monoenergetic *e*-beams. Lanex images of 10 consecutive shots taken with **(a)** plasma density: $2.0 \times 10^{17} \text{ cm}^{-3}$; length: 0.5

mm, and **(b)** plasma density: $1.7 \times 10^{18} \text{ cm}^{-3}$; length: 2 mm. These spectra are part of a larger set used, in the text, to calculate the x-ray beam reproducibility and stability for the lowest and highest energy tuning points of Fig. 3. Each series was chosen to represent the statistics of the data set of which it is a part. The divergence of the beams is recorded in the horizontal axis while the energy is recorded on the vertical axis. **(c)** Individual *e*-beam spectra from the data sets analyzed for Fig. 3. Each shot was chosen to best represent the average *e*-beam energy of the set. The beams are quasi-monoenergetic across the entire tunable range. The accelerator-jet density and length are noted for each image. **(d)** The same *e*-beam central energy data, including error bars, plotted in Fig. 3 is here plotted versus the electron density of the set for 0.5-mm (■) and 2-mm (●) accelerator-jet lengths. The central energy is controlled by the density and length of the accelerator plasma. For both jet lengths, the injector-jet plasma density was kept constant, at $1.7 \times 10^{18} \text{ cm}^{-3}$ and $2.9 \times 10^{18} \text{ cm}^{-3}$, respectively.

Figure S3: Comparison of x-ray spectra measured by the Ross-filter technique.

Spectral measurements obtained with Ross filters: **(a)** polyenergetic x-rays, and **(b)** high-energy monoenergetic x-rays. Experimental data points (■) have been normalized to the spectrum (—) produced by applying a $4\gamma^2 E_L$ scaling to the measured *e*-beam spectrum (inset). The results indicate that the technique can distinguish different spectral shapes.

Figure S4: Photon number stability. The average photon number/shot, measured for each of the points shown in Fig. 3 of the main text, plotted as a function of the average central energy of the x-ray beam. Vertical and horizontal error bars represent the 80%

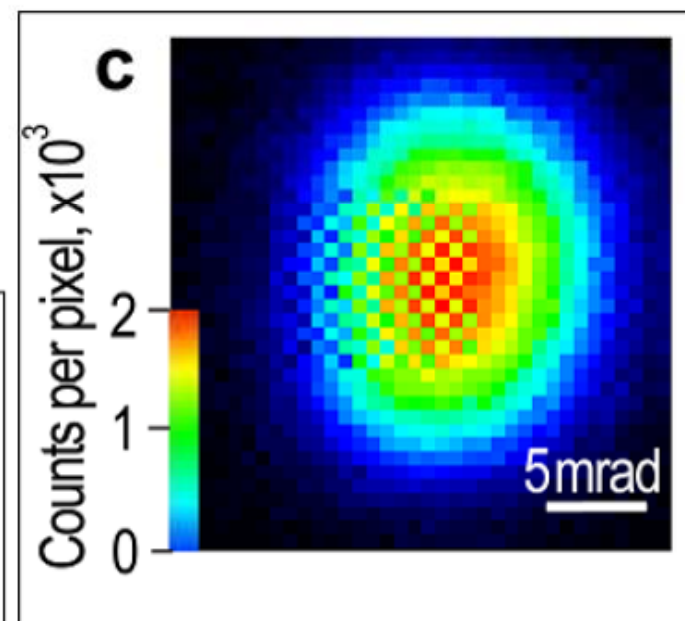
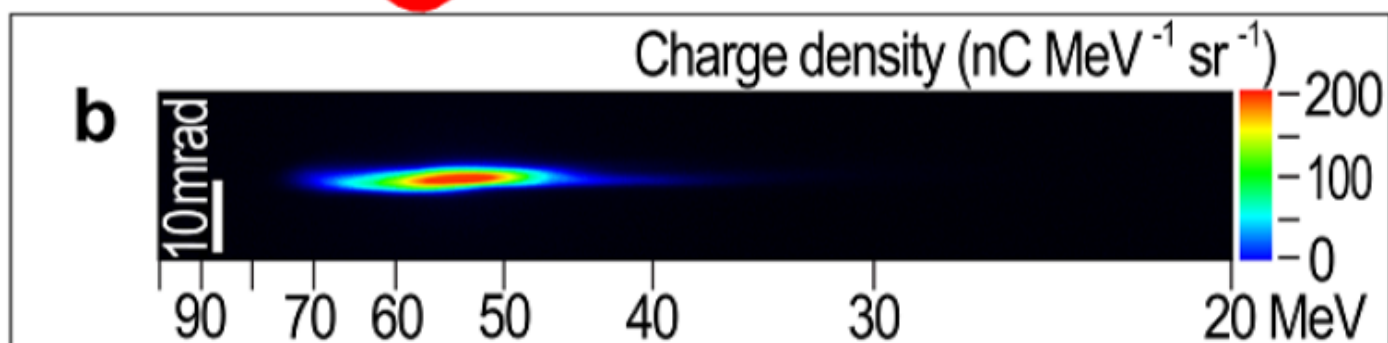
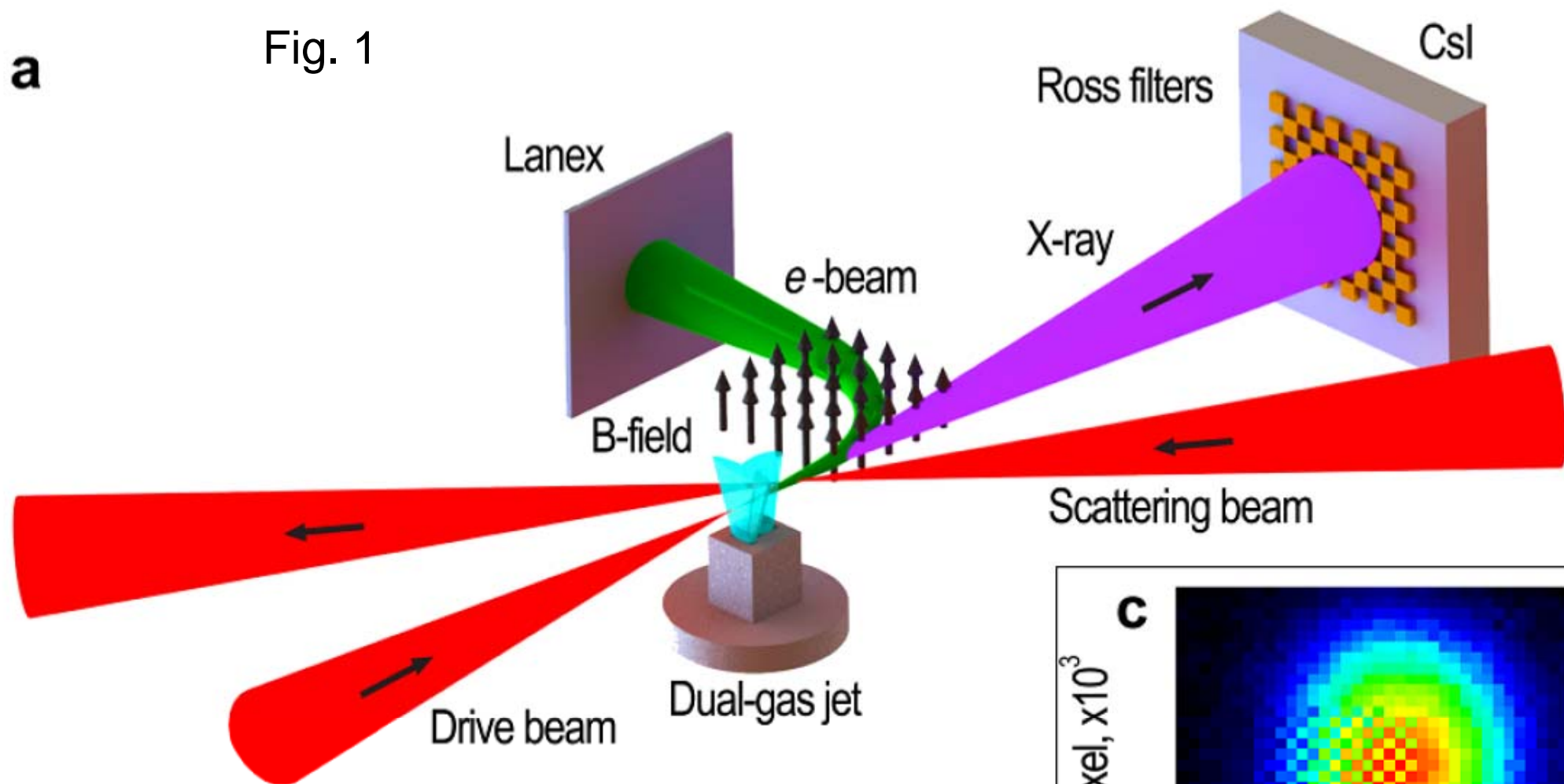
confidence intervals, calculated using t -distribution of shot-to-shot fluctuations in the measured values. Across an order-of-magnitude range of x-ray energy, the x-ray photon number is found to be stable to within 60% of its average value, 1.7×10^6 .

Tables

Ross pair	Filter 1	Filter 2
1	Dy ($96 \pm 1 \mu\text{m}$) Cu ($50 \pm 1 \mu\text{m}$)	Sn ($234 \pm 2 \mu\text{m}$) Cu ($25 \pm 1 \mu\text{m}$)
2	Ta ($41 \pm 1 \mu\text{m}$) Cu ($16 \pm 1 \mu\text{m}$)	Dy ($96 \pm 1 \mu\text{m}$) Cu ($50 \pm 1 \mu\text{m}$)
3	Au ($30 \pm 1 \mu\text{m um}$) Cu ($6 \pm 1 \mu\text{m um}$)	Ta ($41 \pm 1 \mu\text{m}$) Cu ($16 \pm 1 \mu\text{m}$)
4	Pb ($48 \pm 1 \mu\text{m}$)	Au ($30 \pm 1 \mu\text{m}$) Cu ($6 \pm 1 \mu\text{m}$)

Table 1: Ross-filter pairs used for x-ray spectral measurement. Errors represent the sum of both measurement errors, determined from device sensitivity, and variation in filter thickness across the sample.

Fig. 1



Photon density (photons $\text{MeV}^{-1} \times 10^7$)

Fig. 2

Charge density (pc/MeV)

1.2

0.8

0.4

0.0

Electron energy (MeV)

20

40

60

80

1.0

0.8

0.6

0.4

0.2

0.0

20

40

60

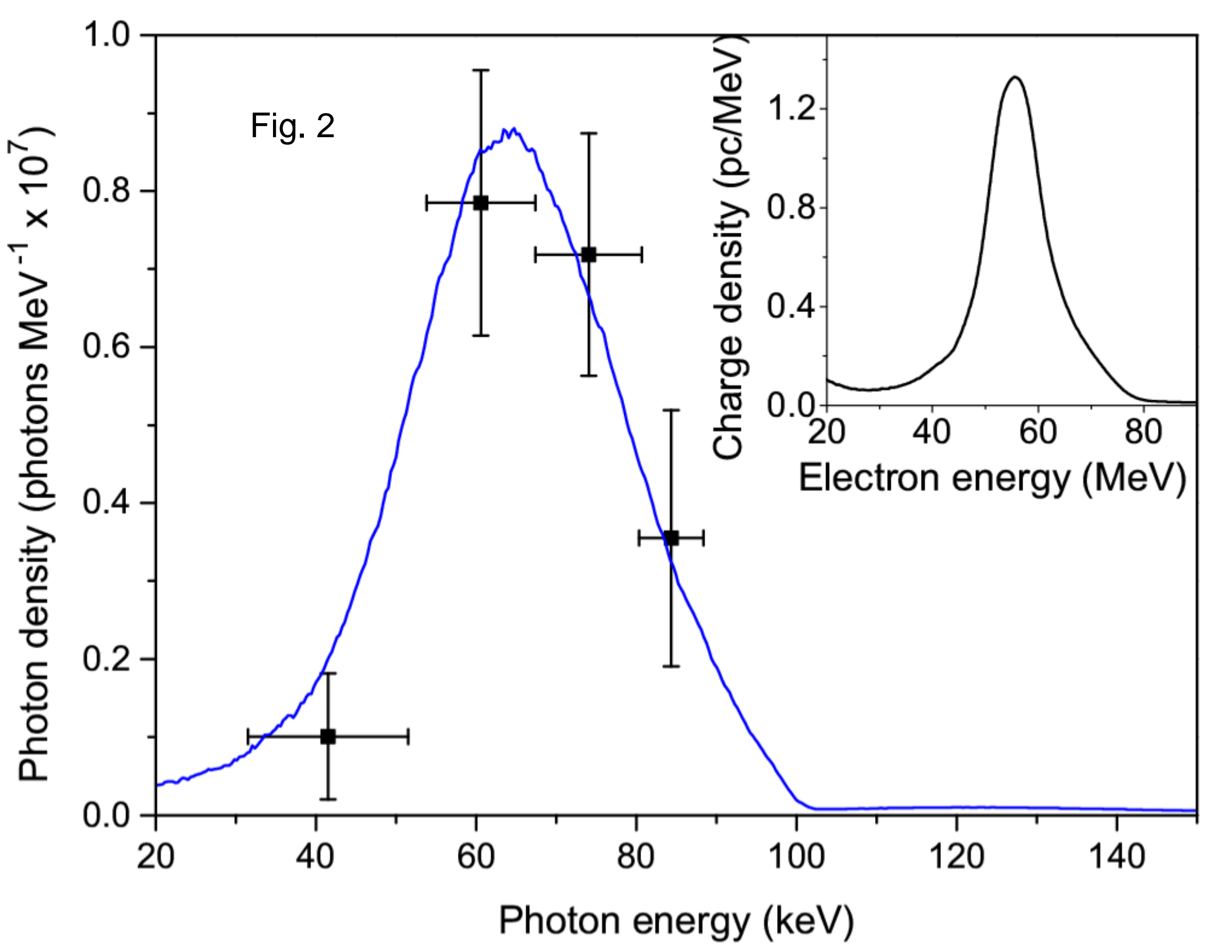
80

100

120

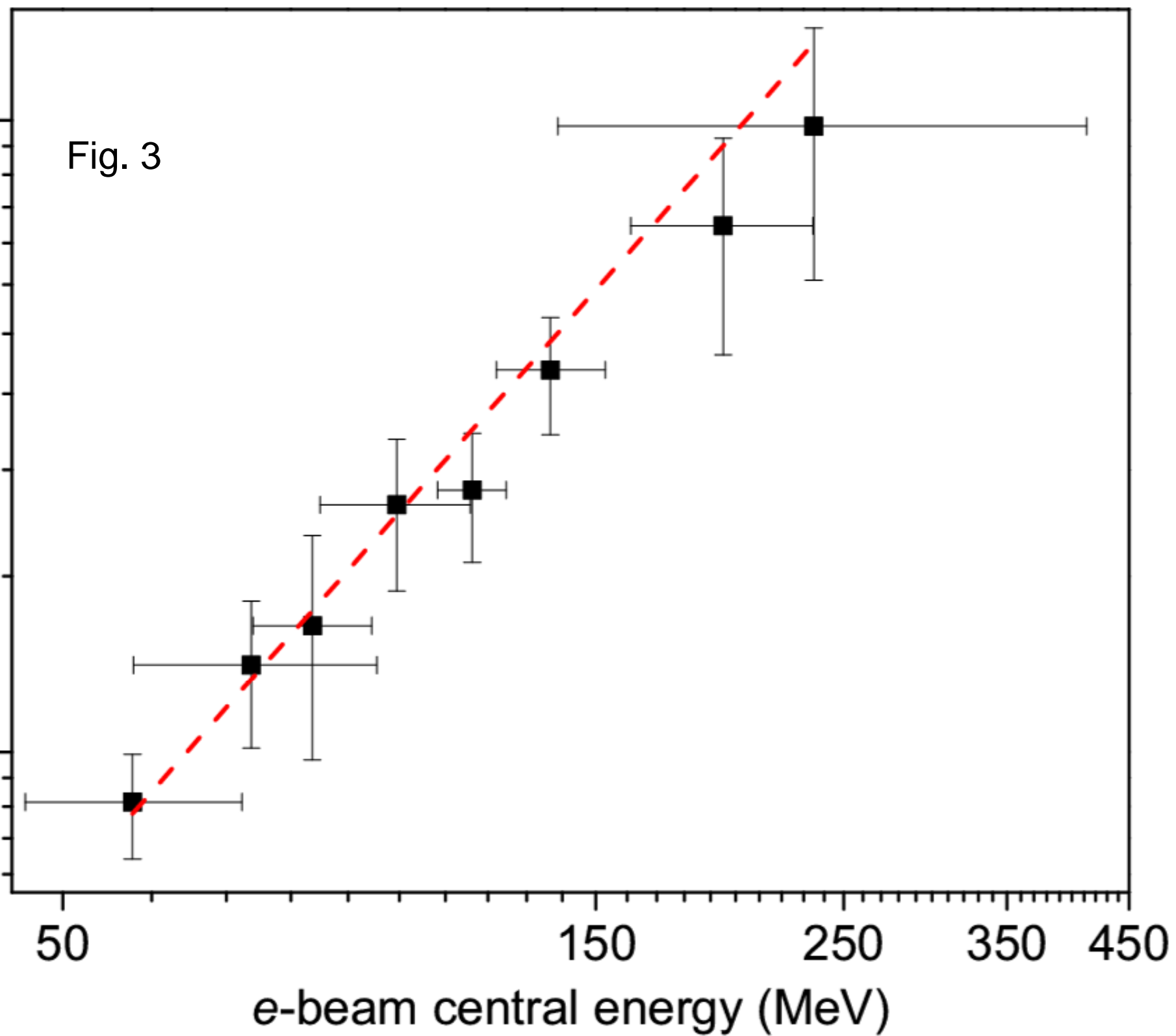
140

Photon energy (keV)

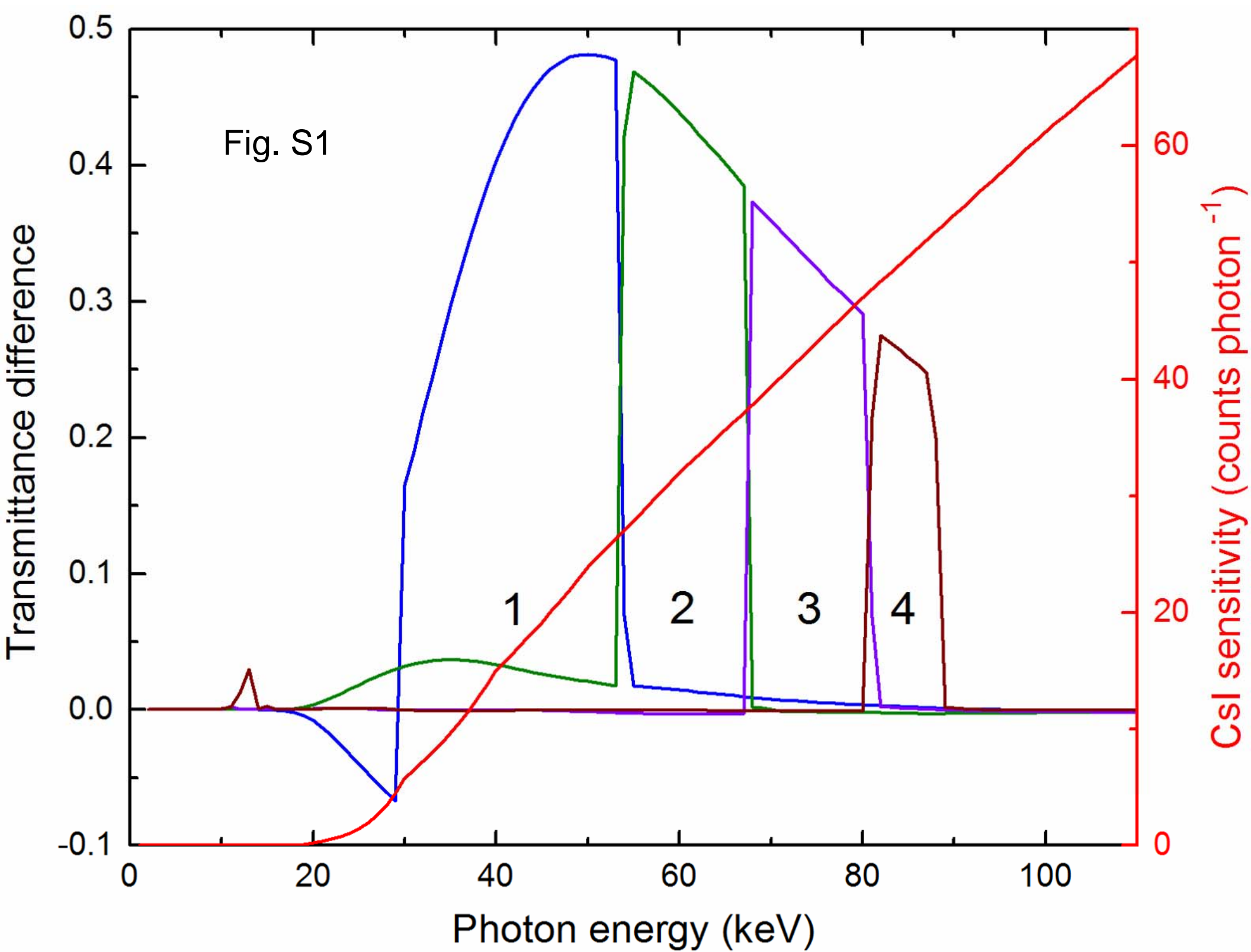


X-ray central energy (keV)

Fig. 3



e-beam central energy (MeV)



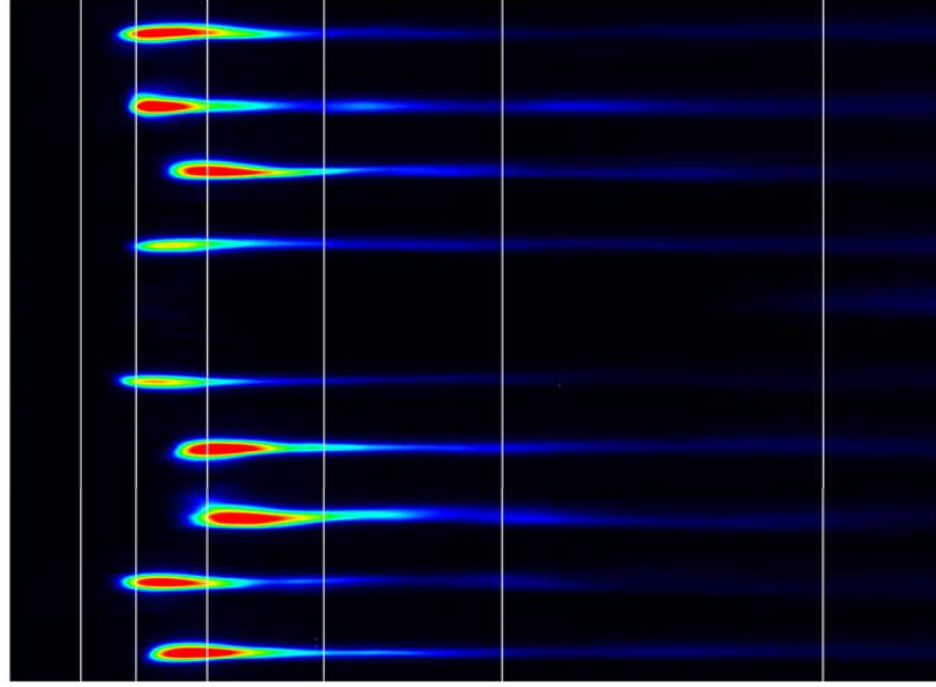
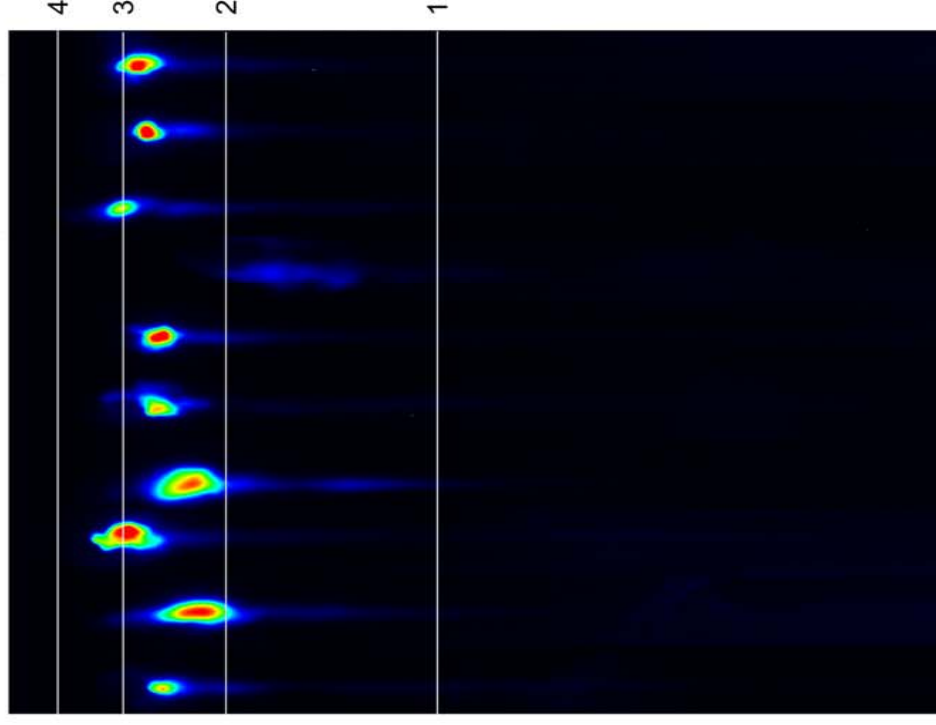
b

Fig. S2



Charge (arb. u.)

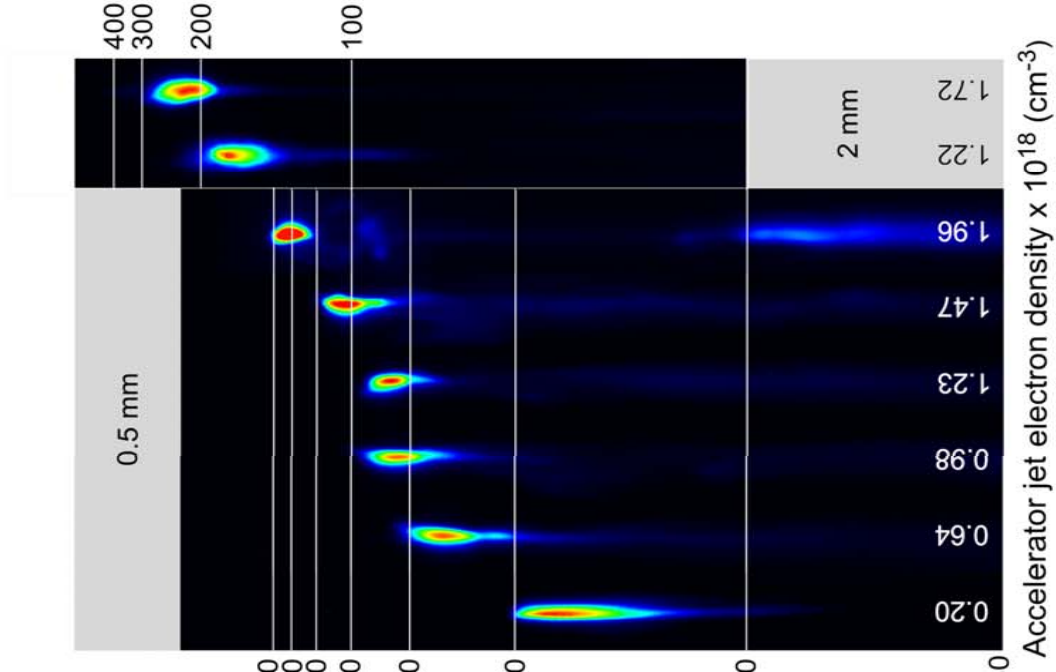
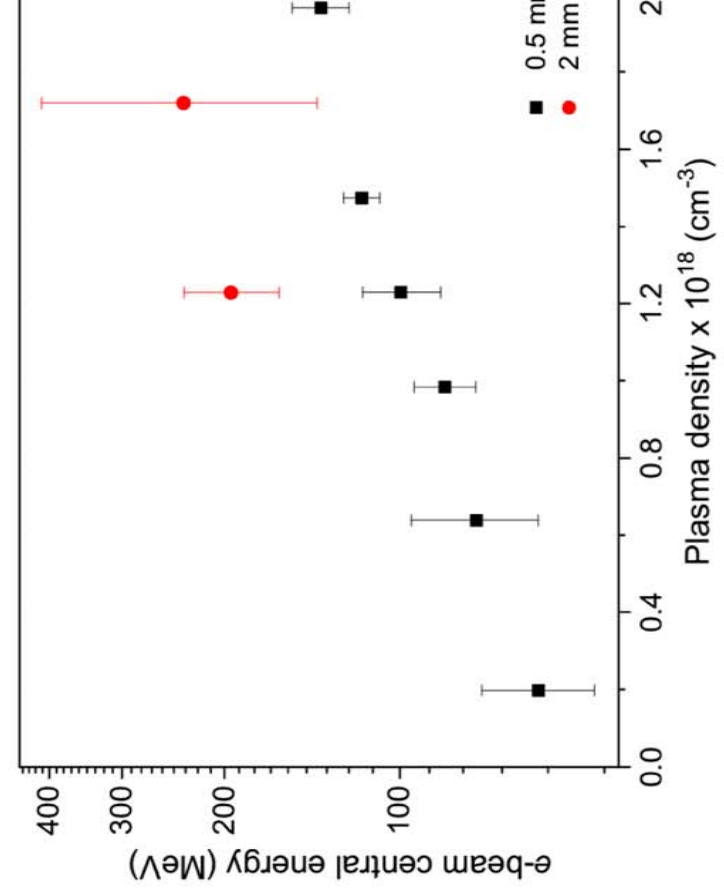
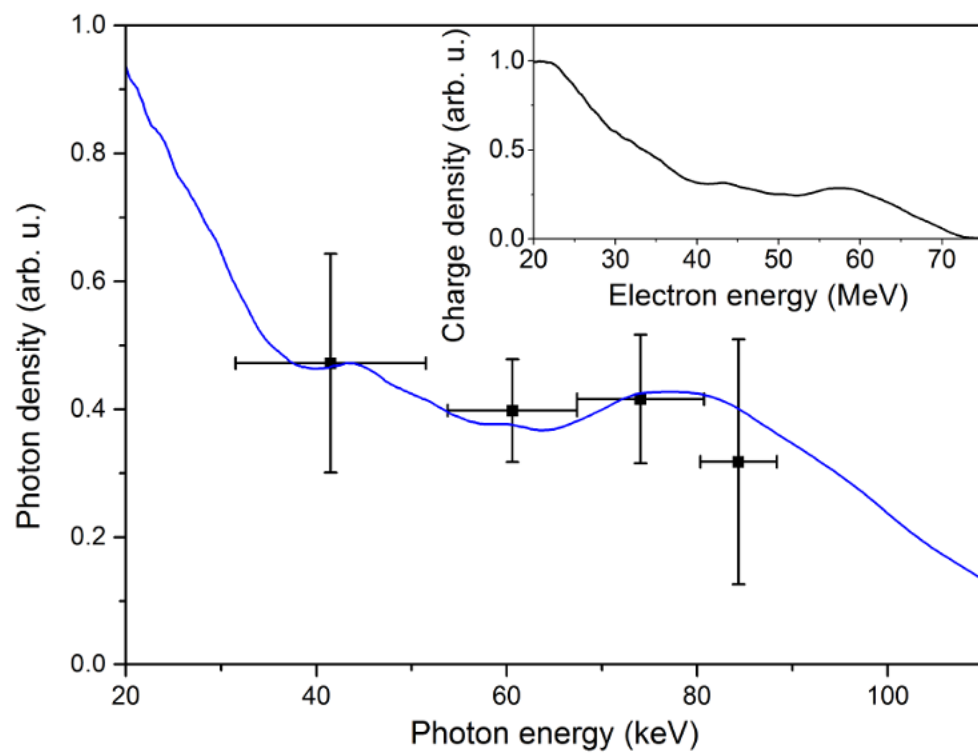
**d**

Fig. S3

a



b

